PERGAMON

International Journal of Heat and Mass Transfer 42 (1999) 2605–2619

International Journal of HEAT and MASS TRANSFER

Frost formation in rotary heat and moisture exchangers

S. Bilodeau, P. Brousseau, M. Lacroix*, Y. Mercadier

Département de Génie Mécanique, Université de Sherbrooke, Sherbrooke, Québec, Canada J1K 2R1

Received 7 August 1997; in final form 15 September 1998

Abstract

Frost formation in rotary heat and mass exchangers is investigated both experimentally and numerically. Experiments reveal that glazed frost, whose density and thermal conductivity are larger than that of rough frost, prevails in rotary exchangers operating in cold climates. A mathematical model for the prediction of the thermal behavior of the exchanger is presented. The model is validated with experimental data and employed to conduct a parametric study. Results indicate that the absolute humidity is the prevailing parameter to characterize the frosting phenomenon. A frost mass fraction chart is established in terms of the relative humidity of the warm exhaust stream and of the temperature of the cold supply stream. The transient three-dimensional model also shows that the absolute humidity and the temperature of both air flows vary nonlinearly in the frosted zone.

Nomenclature

A interfacial surface [m^2]
c_p specific heat [J kg^{-1} K^{-1}]
D diffusion coefficient
FMF frost mass fraction
h heat transfer coefficient [W m^{-2} K^{-1}]
h_m mass transfer coefficient [m s^{-1}]
h^* relative heat of adsorption
H enthalpy [J]
J mass flux [kg m^{-2} s^{-1}]
k heat diffusion coefficient [W m^{-1} K^{-1}]
L width of the matrix [m]
m mass [kg]
$\dot{m}$ mass flowrate [kg s^{-1}]
p pressure [Pa]
r mass generation [kg m^{-3} s^{-1}]
r space coordinate [m]
R radius [m] or gas constant [J kg^{-1} K^{-1}]
RH relative humidity
t time [s]
T temperature [K]
u specific energy [J kg^{-1}]
v velocity [m s^{-1}]
V volume [m^3]
W moisture content [kg desiccant^{-1}].
z space coordinate [m]

Greek symbols

ε volume fraction or effectiveness
θ space coordinate [rad]
ρ density [kg m^{-3}]
ϕ general dependent variable
Ω rotation speed [s^{-1}]
ω specific humidity [kg vapor/kg dry air] or mass fraction [ρ_k/ρ_i]
$\Delta\omega$ vapor concentration gradient between cold surface and air stream.

Subscripts

α solid water
β humid air in the frost layer
γ humid air flow
σ solid matrix
a dry air
ad sorption
CE cold exhaust
CS cold supply
d desiccant
f frost layer
fg evaporation
i component
j component

* Corresponding author. Tel.: 001 819 821 8000; fax: 001 819 821 7163.
E-mail address: marcel.lacroix@gme.usherb.ca (M. Lacroix)

0017–9310/99/$ - see front matter
PII: S0017–9310(98)00323–8

k phase
l liquid water
m matrix
s surface of the matrix
sat saturation
v water vapor
WE warm exhaust
WS warm supply.

1. Introduction

Frosting of heat recovery ventilators (HRV) and rotary heat and moisture exchangers (RHE) is frequently observed in cold climates. Frost builds up when the exhaust air stream from the exchanger is cooled below its dew point and moisture condenses on a cold surface below the freezing temperature. Frosting results in a reduction of the heat transfer rates and an increase of the pressure losses through the heat exchanger.

Frosting of rotary heat exchangers has received little attention in the open literature. Perhaps the paucity of attention devoted to this problem is due to the fact that most of these exchangers operate in climates where frosting rarely occurs. Nevertheless, in northern countries, frosting of RHE is a problem of primary concern [1, 2].

Holmberg [3], Pfeiffer and Hübner [4] and Ruth et al. [5] have conducted experimental studies on the frosting phenomenon during the operation of hygroscopic and non-hygroscopic thermal wheels. Frosting of rotary exchangers has also been investigated numerically by Holmberg [3] and by Attia and D'Silva [6]. In both their models, heat transfer was two-dimensional and the underlying mechanisms of frost formation (such as details of frost layer structure and mass transfer among the phases) were ignored. Stiesh et al. [7] have successfully modelled the annual operation of an RHE in order to calculate the overall performance of commercially available systems. Their model did not, however, account for the phenomenon of frosting formation.

To the authors' knowledge, no thorough analytical or numerical study has been performed so as to allow a deeper understanding of the periodic frosting–defrosting phenomena taking place in rotary exchangers that operate in cold climates. The present paper addresses this problem first by performing experiments in the laboratory and next by developing a mathematical model. The model is validated with the experimental data and then employed to examine the global performance of the RHE in frosting conditions and to predict both the frosting limit and the impact of frost formation on the RHE thermodynamic behavior.

2. Experimental investigations

Two experimental investigations were conducted in order to make some observations on the frosting phenomenon and to generate data for model validation. The phenomenon of frosting on a refrigerated plate was first examined in order to determine the type of frost that prevails under typical operating conditions of RHE in cold climates. Next, the effect of frost formation on the performance of a rotary exchanger was measured for a few test cases. The results of these experiments will later be used for validating the theoretical model presented in Section 3.

2.1. Type of frosting on a refrigerated surface

Frost formation on a cold surface has been investigated by Hayashi et al. [8] as well as by Tao et al. [9] and Tokura et al. [10]. These investigators observed the fundamentals of frosting on a cold surface. Our experimental investigation is concerned with the frost formation corresponding to RHE's operating conditions. The experimental set-up consists of a digital camera coupled to a microscope and mounted above a refrigerated metallic plate allowing pictures to be taken while frosting is taking place.

The key parameters here are the refrigerated plate surface conditions (roughness and surface temperature T_s) and the water concentration difference above the plate $\Delta\omega$ [8–10]. Experimental observations have revealed that the phenomenon of frost formation may be divided into three distinct phases: the nucleation phase, the frost formation phase and the frost layer growth phase. These three phases are illustrated in Fig. 1a–c, respectively. First, the nucleation phase lasts for a few tens of s. Liquid droplets condense and coalesce along the scratches on the refrigerated surface and begin to freeze. Figure 1a shows the nucleation process at 25 s for $T_a = 22^\circ C$, $\phi_a = 40\%$, $T_m = -15^\circ C$ and a magnification of $400\times$. Next, in the frost formation phase, frost columns appear and grow in size. Figure 1b exemplifies frost columns at 95 s for $T_a = 22^\circ C$, $\phi_a = 50\%$, $T_m = -10^\circ C$ and a $400\times$ magnification. In the last phase, i.e. the frost layer growth phase, a sufficiently large number of frost columns have accumulated so to yield a porous medium frost layer which grows with time. Figure 1c illustrates such a layer.

As the frost layer thickens, the thermal resistance increases and the frost surface temperature rises to reach a constant value close to $0^\circ C$ at a standard atmospheric pressure. Figure 2a shows that its thickness increases quasi linearly with time. Both the cold surface temperature and the air moisture content not only have a significant effect on the resulting thickness and density of the frost layer but also on the type of frost. A low surface temperature yields frost layers of low density while high air moisture contents lead to higher densities. It was found that after an initial growth period, the mean diameter of the frost layer columns reaches a constant value (Fig. 2b). This behavior explains why, from that point

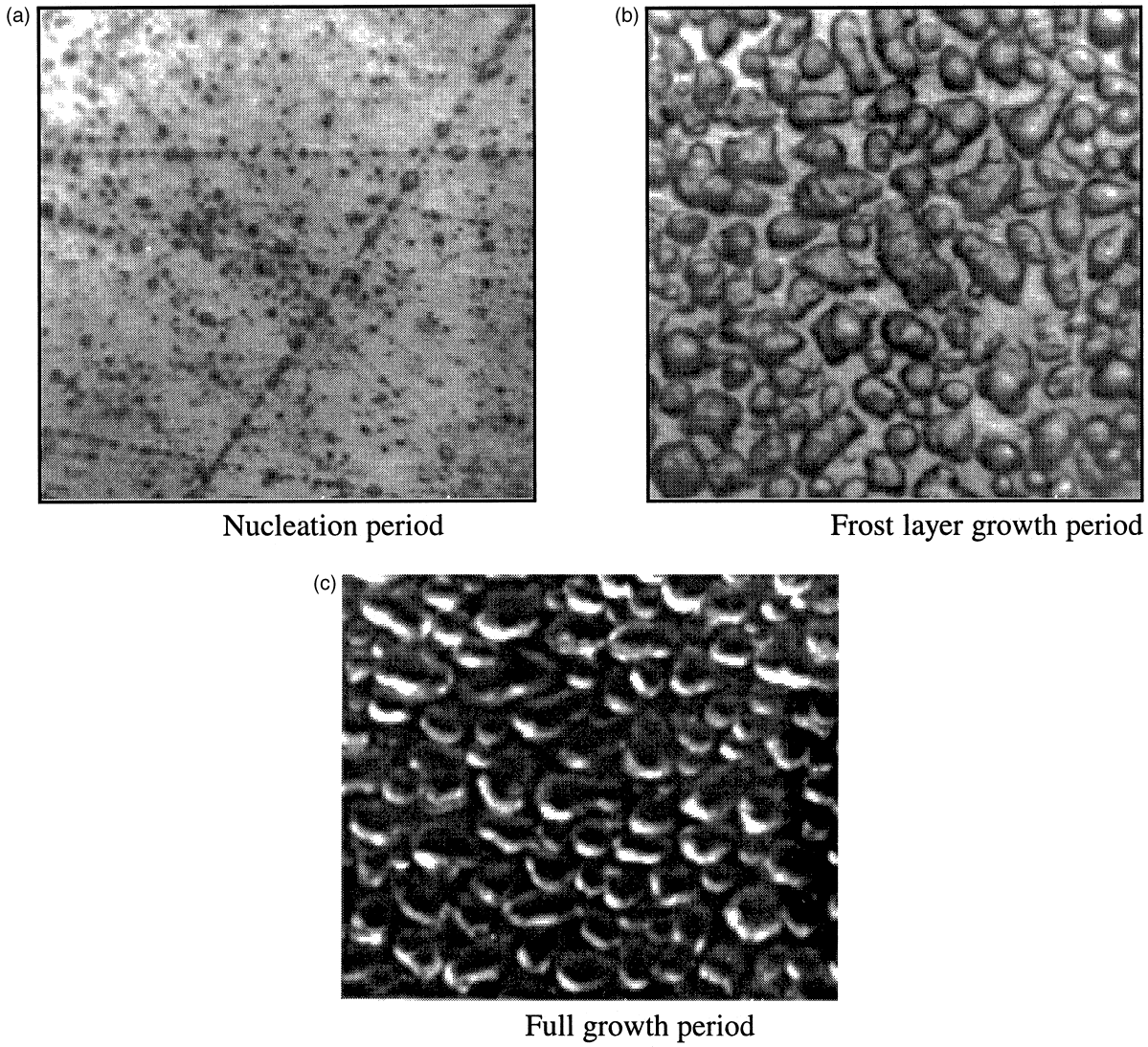

Fig. 1. (a) Nucleation period. (b) Frost layer growth period. (c) Full growth period.

on, the thickness of the frost layer increases linearly with time.

Figure 3 summarizes the main results obtained with the refrigerated plate set-up and used to define the theoretical model. As shown in this figure, two types of frost were observed. The first type, referred to as rough frost, occurs when heat and mass transfer are important i.e. when T_s and $\Delta\omega$ are low. The second type, referred to as glazed frost, occurs when heat and mass gradients are small. These types of frost exhibit very different formation rates. Rough frost grows rapidly while glazed frost grows slowly. As a result, the density and the thermal conductivity of glazed frost (and so its effect on the operation of exchangers) are larger than that of rough frost. Our results (Fig. 3 illustrates those of Hayashi et al. [8] and Östin et al. [11]) have shown that, for typical operating conditions of RHE in cold climates, glazed frost predominates.

2.2. Experimental apparatus to validate the theoretical model

The second experiment is concerned with the frost formation in a rotary exchanger operating in conjunction with a total energy recovery ventilation system. Results for this experiment will later be employed for the validation of the theoretical model. The experimental setup consists of a hygroscopic thermal wheel installed in an enthalpy recovery ventilator system. The test chamber controls the climatic conditions of the cold air supply

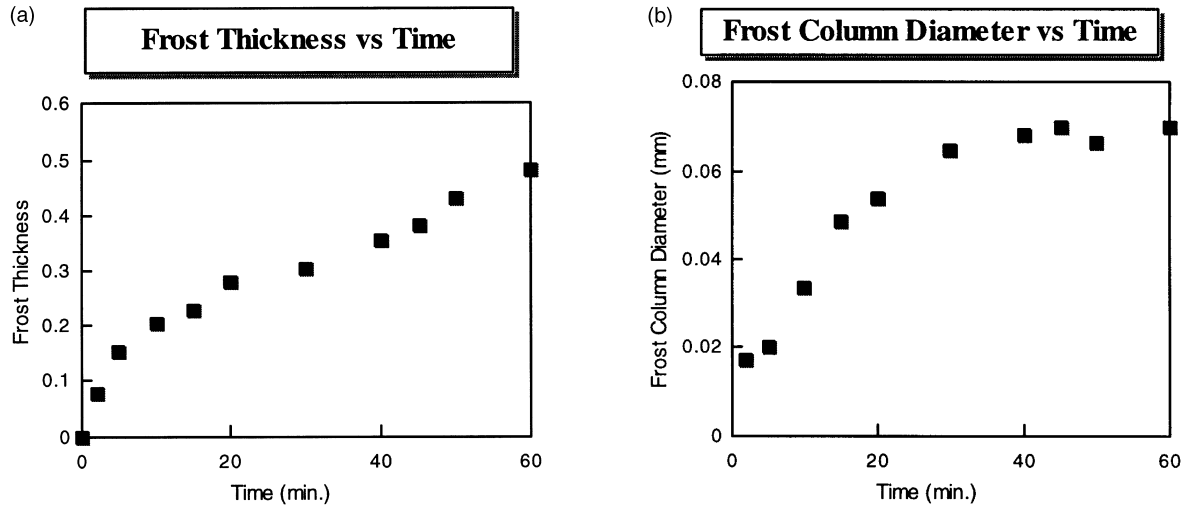

Fig. 2. (a) Frost thickness vs time. (b) Frost column diameter vs time.

whereas the exhaust air stream conditions are maintained by an independent furnace and humidifier. Operating conditions range from -30 to $-40^{\circ}C$ with dew point temperature ranging from -30 to $20^{\circ}C$, and air flow rates up to $80\,l\,s^{-1}$. The mean inlet and outlet temperature are measured by four copper constantan thermocouples. The specific humidity of the inlet and outlet air streams are also recorded with the help of four dew point meters of $\pm 0.5^{\circ}C$ accuracy. The inlet and outlet temperatures of the air streams passing through the hygroscopic wheel are measured by an array of 20 uniformly distributed thermocouples connected to a data acquisition system.

Hygroscopic air-to-air rotary heat exchangers transfer energy in both sensible and latent heat forms in a periodic adsorption–regeneration cycle (Fig. 4). In the adsorption part, the dew point decreases as the exhaust air stream flows through the microchannels and gives off water to the desiccant. In the regeneration part, the desiccant releases its humidity to the stream of dry air. Since the moisture content of the air decreases significantly in the

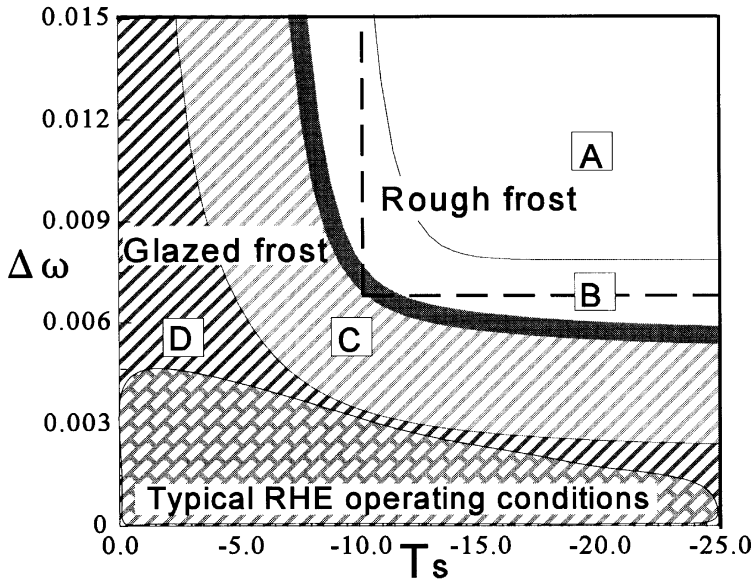

Fig. 3. Thermokinetics and frost categories.

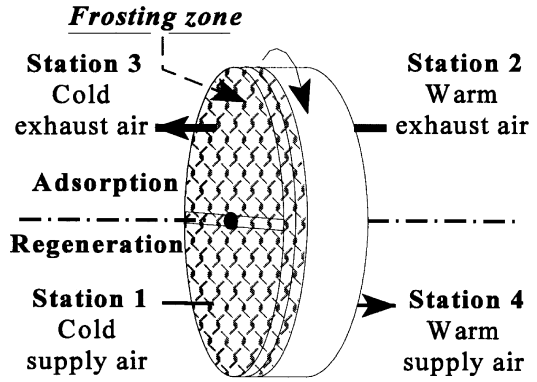

Fig. 4. Frosting of rotary heat and moisture exchanger.

cold region of the rotor, it is observed that the frosting limit is lower for the rotary exchanger than that for the plate exchanger [3–5]. Over time, the density of the frost layer tends to increase up to an asymptotic value (which depends on operating conditions). The cyclic nature of the RHE seems to be the main cause for frost layer densification since parts of this layer cycles around its melting point and near the psychometric saturation temperature.

In order to model frost formation, a frosting criterion was established based on experimental observations. First, it is assumed that moisture condensing out of the air on the rotor surface will be in the form of frost when the surface temperature is below the freezing point. Second, if the air flow is saturated, it is unable to pick up all frost on sublimation, and the excess water will form as a frost layer. Mathematically, frosting is triggered when the following conditions are fulfilled:

$$T_s < 0 \quad \text{and} \quad \Delta\omega = \omega_\gamma - \omega_s > 0. \tag{1}$$

The initial thermophysical and mechanical properties of the frost layer are then evaluated with the help of experimental data (column diameter, density, thickness) [9–11]. It must be pointed out that a frost layer will grow in thickness and density if the mean temperature during one revolution at a cross section of the rotor remains below 0°C.

3. Mathematical model

A mathematical model of a hygroscopic rotary regenerator under frosting conditions was developed. The transient three-dimensional multiphase flow equations were derived for a representative control volume (RCV) of the rotor [12, 13]. The RCV, as shown in Fig. 5, may contain three constituents: humid air (γ), a frost layer (f), and a hygroscopic matrix (σ). These constituents are composed of additional components. For instance, humid air flow comprises dry air (a) and water vapor (v). The frost layer consists of ice (α) and of confined humid air (β). This latter is a mixture of dry air (af) and of water vapor (vf). Finally, the hygroscopic matrix consists of a solid matrix with a desiccant layer (d) and liquid water (l).

In the RCV, it is assumed that the frost layer is a homogeneous porous medium with a uniform density. However, the frost properties are assumed to be time dependent. They are evaluated during the initial frost layer formation period and also during the full growth period. A previous paper has shown that neglecting the initial frost layer formation period leads to poor predictions of the frost density and conductivity [9]. Furthermore, the following assumptions are adopted in the present model:

- The thermophysical and the flow properties of the inlet streams are constant and uniform.

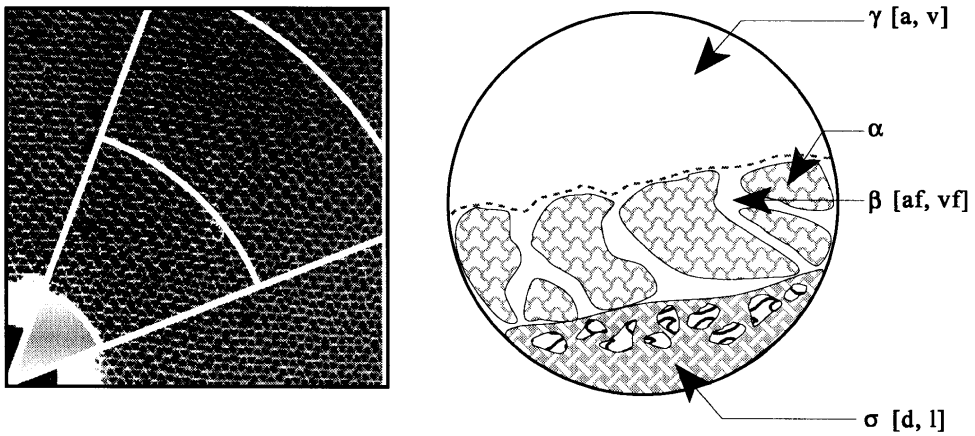

Fig. 5. Representative control volume (RCV).

- The regenerator is considered adiabatic with respect to the environment.
- Pressure drops in the axial flow are negligible with respect to the total pressure; the total pressure of the gaseous phases (β and γ) remains constant.
- The frost layer and the desiccant matrix are in thermodynamic equilibrium.
- Gas-phase convection in the frost layer is negligible compared with molecular diffusion.
- Radiation is negligible with respect to the interphase convection.
- Both humid air phases (β and γ) are assumed incompressible.
- The desiccant matrix remains solid and at rest; the volume fraction of the matrix is constant.

Based on the foregoing assumptions, the mass and energy conservation equations for a constituent k in phase i may be stated as

$$\frac{\partial \bar{\rho}_{k,i}}{\partial t} + \nabla\cdot(\omega_{k,i}\bar{J}_i) + \nabla\bar{j}_{k,i} - \sum_{ij} r_{k,ij} = 0 \tag{2}$$

and

$$\sum_k \frac{\partial}{\partial t}(\bar{\rho}_k H_k) + \sum_k \nabla\cdot[H_k(\omega_{k,i}\bar{J}_i + \bar{j}_{k,i})] = -\sum_k \nabla\cdot q_k + R_{\mathrm{h}_i}. \tag{3}$$

The first term in equation (2) represents the mass accumulation. The second and third terms stand for convection and diffusion respectively. The last term is the mass accumulation rate of k in phase i due to interphase transfer. These terms are characterized by the mean convective flux (J), the mass diffusion flux (j) given by Fick's law and the mass accumulation rate ($r_{k,ij}$):

$$\bar{J}_i = \bar{\rho}_i v_i; \quad \bar{j}_k = -\rho_i D_{ki}\nabla\omega_{ki}; \quad r_{k,ij} = \frac{A_{ij}}{V} h_{mij}(\rho_{k,j} - \rho_{k,i}). \tag{4}$$

The last relation is established in conformity with Gibbs Law, which stipulates that $r_{k,ij} = 0$ if the chemical potential of the kth component in phase i is the same as its own chemical potential in phase j.

The energy conservation equation (3) also exhibits an accumulation term and a convective term. The heat diffusion term is given by Fourier's law and heat generation (R_{h_i}) is given by

$$R_{\mathrm{h}_i} = \frac{A_{ij}}{V} h(T_i - T_j). \tag{5}$$

The j subscript in the last equation represents the surface in contact with the air flow. If no frost has been formed on the surface of the matrix, then the subscript ij represents the interfacial surface between the air flow and the matrix. On the other hand, if the surface is frosted or if the frosting criterion is met, ij represents the interface between the air flow and the frost layer.

Equation (3) may be rewritten in terms of temperature and concentration:

$$\frac{\partial T_i}{\partial t} + v_i\nabla T_i = \nabla\left(\frac{\sum_k \bar{k}_k}{\bar{\rho}_i c_{\mathrm{p}_i}}\right)\nabla T_i + \left[\frac{R_{\mathrm{h}_i} - \sum_k\left(\sum_{ki} r_{ki}\right)H_k}{\bar{\rho}_j c_{\mathrm{p}_i}}\right] + \sum_k\left(\frac{D_{ki}}{\omega_{k,i}}\nabla\omega_{k,i}\right)\nabla T_i. \tag{6}$$

The mass and energy equations are volume average equations, and their intensive properties are evaluated as follows:

$$\bar{\rho}_i = \varepsilon_i\rho_i; \quad \bar{J}_i = \varepsilon_i J_i; \quad \bar{j}_i = \varepsilon_k j_j \tag{7}$$

ε_i is defined as the nondimensional volume fraction of the constituent i, and it represents the ratio of the volume occupied by the constituent i to the RCV volume. The axial geometry of the RHE implies that a surface fraction (perpendicular to the flow) is identical to the corresponding volume fraction. Consequently, the sum of the volume fractions of all components is equal to one and ε_i may be used to evaluate the intensive surface flux (J and j).

The mass conservation equation (2) may be expanded for each constituent i.e. for the matrix components, for the humid air flow and for the frost layer. The results of this expansion are summarized in Table 1.

The energy conservation equation (6) is expanded for the three constituents i.e. the matrix, the humid air flow and the frost layer. The results of this expansion are provided in Table 2.

The volume fractions of each phase are evaluated as follows:

$$\frac{\partial\varepsilon_{\mathrm{l}}}{\partial t} = \frac{1}{\rho_{\mathrm{l}}}\frac{\partial\bar{\rho}_{\mathrm{l}}}{\partial t} \tag{8}$$

$$\frac{1}{\varepsilon_\gamma}\frac{\partial\varepsilon_\gamma}{\partial t} = \frac{P_{\mathrm{v}}}{P_\gamma}\frac{1}{\bar{\rho}_{\mathrm{v}}}\frac{\partial\bar{\rho}_{\mathrm{v}}}{\partial t} + \frac{1}{T_\gamma}\frac{\partial T_\gamma}{\partial t} \tag{9}$$

$$\frac{\partial\varepsilon_\beta}{\partial t} = \frac{R_\beta}{P_\beta}\left(\bar{\rho}_\beta\frac{\partial T_\beta}{\partial t} + T_\beta\frac{\partial\bar{\rho}_{\mathrm{vf}}}{\partial t}\right) \tag{10}$$

$$\frac{\partial\varepsilon_\alpha}{\partial t} = \frac{1}{p}\frac{\partial\bar{\rho}_\alpha}{\partial t}. \tag{11}$$

Ideal gas law is used to relate gaseous phase state properties. Additional relations needed to close the system of equations are the adsorption isotherm

$$P_{\mathrm{v}_i} = \frac{R\rho_{\mathrm{l}}P_{\mathrm{v}_{\mathrm{sat}}}(T_{\mathrm{m}})}{\rho_{\mathrm{l}_{\max}} + (R-1)\rho_{\mathrm{l}}}\left[\frac{P_{\mathrm{v}_{\mathrm{sat}}}(T_{\mathrm{m}})}{P_{\mathrm{v}_{\mathrm{sat}}}(T_0)}\right]^{(h^*-1)} \tag{12}$$

and the Clapeyron equation

$$\left(\frac{\mathrm{d}P}{P}\right)_{\mathrm{sat}} = \frac{h_{\mathrm{fg}}}{R}\left(\frac{\mathrm{d}T}{T^2}\right)_{\mathrm{sat}}. \tag{13}$$

The boundary conditions for the above conservation equations may be stated as follows:

Table 1
Parameters for the mass conservation equations

Constituent		ρ	J_{adv}	J_{dif}	r_{ij}
Desiccant matrix	Dry matrix	d	0	0	0
	Liquid water	1	0	$\bar{\rho}_d D_{ld} \nabla \bar{\rho}_l$	$\frac{A_{\sigma\gamma}}{V} h_{m\sigma}(\rho_{l\gamma} - \rho_l)$
Humid air flow	Dry air	a	$\rho_\gamma v_\gamma$	0	0
	Water vapor	v	$\rho_\gamma v_\gamma$	0	$\frac{A_{\gamma j}}{V} h_{m_{\gamma j}}(\rho_{vj} - \rho_v)$
Frost layer	Ice	α	0	0	$\frac{A_{\gamma f}}{V} h_{mf} \varepsilon_{\alpha f}(\rho_{\alpha\gamma} - \rho_\alpha)$
	Dry air	af	0	0	0
	Water vapor	vf	0	$\frac{D_{av}}{\tau_f}\left(1 - \frac{\rho_f}{\rho_{ice}}\right)\nabla \bar{\rho}_v$	$\frac{A_{\gamma f}}{V} h_{mf} \varepsilon_{\beta f}(\rho_{vf\gamma} - \rho_{vj})$

Table 2
Parameters for the energy conservation equations

Constituent	T	Adv.	Diffusion	Interphase transfer
Desiccant matrix	σ	0	$\left\langle \frac{\sum_k \bar{k}_k}{\bar{\rho}_\sigma c_{p_\sigma}} \right\rangle \nabla T$	$\frac{A_{\sigma\gamma}}{V}\left[\frac{h(T_\sigma - T_\gamma)}{\bar{\rho}_\sigma c_{p_\sigma}} - \frac{h_{m\sigma}(\rho_{l\gamma} - \rho_l) H_l}{\bar{\rho}_\sigma c_{p_\sigma}}\right]$
Humid air flow	γ	${}_\gamma\nabla T$	0	$\frac{\frac{A_{\gamma j}}{V}[h(T_\gamma - T_j) - h_{mj}(\rho_{vj} - \rho_v) H_v]}{\bar{\rho}_\gamma c_{p_\gamma}}$
Frost layer	f	0	$7\left\langle \frac{\sum_k \bar{k}_k}{\bar{\rho}_f c_{p_f}} \right\rangle \nabla T$	$\frac{i(T_f - T_\gamma) - h_{mf}\varepsilon_{\alpha f}(\rho_{\alpha\gamma} - \rho_\alpha) H_\alpha - h_{mf}\varepsilon_{\beta f}(\rho_{vf\gamma} - \rho_{vj})}{\bar{\rho}_f c_{p_f}}$

For the desiccant matrix, $\sum_k \bar{k}_k = \varepsilon_l k_l + \varepsilon_d[k_m(1 + f_{ads}) + k_{ads} f_{ads}]$.
For the frost layer, $\sum_k \bar{k}_k = \varepsilon_\alpha k_\alpha + \varepsilon_\beta \frac{k_{vf}\bar{\rho}_{vf} + k_a \bar{\rho}_a}{\bar{\rho}_\beta}$

At the circumferential limit of the wheel, $r = r_o$ and $0 < z < L$,

$$\frac{\partial \rho_l}{\partial r} = \frac{\partial \rho_v}{\partial r} = \frac{\partial \rho_{vf}}{\partial r} = \frac{\partial \rho_\alpha}{\partial r} = \frac{\partial T_a}{\partial r} = \frac{\partial T_m}{\partial r} = \frac{\partial T_f}{\partial r} = 0. \quad (14)$$

At the inlet of the regeneration section,

at $z = 0$; $\quad r_i \leqslant r \leqslant r_o$

$$\Omega t \leqslant \theta \leqslant \Omega t + \pi$$

$$\rho_v = \rho_v|_{reg,in}; \quad \frac{\partial \rho_l}{\partial z} = \frac{\partial \rho_{vf}}{\partial z} = \frac{\partial \rho_\alpha}{\partial z} = 0$$

$$\frac{\partial T_m}{\partial z} = \frac{\partial T_f}{\partial z} = 0; \quad T_a = T_{a,cs}. \quad (15)$$

At the inlet of the adsorption section,

at $z = L$; $\quad r_i \leqslant r \leqslant r_o$

$$\Omega t \leqslant \theta \leqslant \Omega t + \pi$$

$$\rho_v = \rho_v|_{ads,in}; \quad \frac{\partial \rho_l}{\partial z} = \frac{\partial \rho_{vf}}{\partial z} = \frac{\partial \rho_\alpha}{\partial z} = 0$$

$$\frac{\partial T_m}{\partial z} = \frac{\partial T_f}{\partial z} = 0; \quad T_a = T_{a,we} \quad (16)$$

and at the outlet of the wheel,

$$\frac{\partial \rho_l}{\partial z} = \frac{\partial \rho_v}{\partial z} = \frac{\partial \rho_{vf}}{\partial z} = \frac{\partial \rho_\alpha}{\partial z} = \frac{\partial T_a}{\partial z} = \frac{T_m}{\partial z} = \frac{\partial T_f}{\partial z} = 0. \quad (17)$$

Equations (2)–(6) may be cast in the following standard form

$$\frac{\partial \phi}{\partial t} + v \cdot \nabla \phi = \nabla \phi = \nabla \cdot [\Gamma \nabla \phi] + S_\phi \quad (18)$$

where ϕ is the general dependent variable which stands

Table 3
Parameters of equation (19)

ϕ	v	Γ	S_c	S_p
ρ_l	0	0	$\frac{A_{\sigma\gamma}}{V}h_{m\sigma}\rho_{l\gamma}+\bar{\rho}_d D_{ld}\nabla\bar{\rho}_l$	$-\frac{A_{\sigma\gamma}}{V}h_{m\sigma}$
ρ_v	$+\mathbf{vk}$(reg)/$-\mathbf{vk}$ (ads)	0	$\frac{A_{\gamma j}}{V}h^0_{m_{\gamma j}}\rho_{vj}$	$-\frac{A_{\gamma j}}{V}h_{m_{\gamma j}}$
ρ_α	0	0	$\frac{A_{\gamma f}}{V}h^0_{mf}\varepsilon_{\alpha f}\rho_{\alpha\gamma}$	$\frac{A_{\gamma f}}{V}h_{mf}\varepsilon_\alpha$
ρ_{vf}	0	0	$\frac{A_{\gamma f}}{V}h_{mf}\varepsilon_{\beta f}\rho_{vf\gamma}+\frac{D_{av}}{\tau_f}\left(1-\frac{\rho_f}{\rho_{ice}}\right)\nabla\bar{\rho}_{vf}$	$\frac{A_{\gamma f}}{V}h_{mf}\varepsilon_\beta$
σ	0	$\frac{\sum_k \bar{k}_k}{\bar{\rho}_\sigma c_{p_\sigma}}$	$\frac{A_{\sigma\gamma}}{V}\left[\frac{hT_\gamma}{\bar{\rho}_\sigma c_{p_\sigma}}-\frac{h_{m\sigma}(\rho_{l\gamma}-\rho_l)H_l}{\bar{\rho}_\sigma c_{p_\sigma}}\right]$	$\frac{A_{\sigma\gamma}}{V}\frac{h}{\bar{\rho}_\sigma c_p}$
γ	$\mathbf{vk}$ (reg)/$-\mathbf{vk}$ (ads)	0	$\frac{\frac{A_{\gamma j}}{V}[hT_j-h_{mj}(\rho_{vj}-\rho_v)H_v]}{\bar{\rho}_\gamma c_{p_\gamma}}$	$\frac{A_{\gamma j}}{V}\frac{h}{\bar{\rho}_\gamma c_p}$
f	0	$\frac{\sum_k \bar{k}_k}{\bar{\rho}_f c_{p_f}}$	$\frac{hT_\gamma-h_{mf}\varepsilon_{\alpha f}(\rho_{\alpha\gamma}-\rho_\alpha)H_\alpha-h_{mf}\varepsilon_{\beta f}(\rho_{vf\gamma}-\rho_{vf})}{\bar{\rho}_f c_{p_f}}$	$-\frac{A_{\gamma f}}{V}\frac{h}{\bar{\rho}_f c_p}$

for the mass and the temperature components, Γ is the generalized diffusion coefficient and S_ϕ is a source term that may be linearized as $S_\phi = S_c + S_p\phi$. The dependent variables, velocity components and coefficients are provided in Table 3. Equations (2)–(6) along with their boundary conditions (14)–(17) were solved using a finite-difference method [14]. The resulting finite-difference scheme has the form

$$a_P\phi_P = a_E\phi_E + a_W\phi_W + a_N\phi_N + a_S\phi_S + a_T\phi_T + a_B\phi_B + b \tag{19}$$

where b is the source term. Expressions for the coefficients a in equation (19) may be found in the Appendix. Equation (19) is solved iteratively for ρ_v, ρ_l, ρ_{vf}, ρ_α, T_a, T_m and T_f with a SOR method. Convergence at a given time step is declared when the largest residual for all difference equations is smaller than 10^{-4}. Furthermore the conservation of mass and energy is checked at each iteration. More stringent convergence criteria were retained but the results did not show perceptible changes in the solutions. The overall algorithm of the calculation procedure is depicted in Fig. 6.

4. Results and discussion

The foregoing computational methodology was thoroughly tested for heat and mass transfer in a RHE and the results were compared to those of Attia and D'Silva [6]. These validation exercises are reported in reference [12] and need not be repeated here. To further check the accuracy of the model, the numerical predictions were also compared to the data generated from the experiments described in Section 2.2 [15]. A comparison between the outlet temperature and absolute humidity for the warm supply (WS) and the cold exhaust (CE) is provided in Fig. 7a and b. Operating conditions for the experiments are summarized in Table 4. The numerical simulations were carried out with a grid size of $30\times6\times30$ nonuniformly distributed nodes in the θ–r–z direction respectively and a time step of 0.03125 s. The time step was chosen so as to match the rotational speed of the wheel (16 rpm) with the mesh size in the θ direction. Calculations were conducted on an IBM RISC-6000 station, model 375, and the CPU time averaged 48 h for the simulation of 1 h of heat and mass transfer processes in an RHE. These figures reveal that the numerical predictions are in good agreement with the experimental results. The predicted temperatures and humidities stay within the uncertainty of the measurements.

Next a series of numerical simulations was conducted: (1) to study the overall performance of RHE under frosting conditions, (2) to predict the local thermodynamic properties, and (3) to establish a frosting limit.

Figure 8a and b exemplify the effect of the mass flow rate of air and of the RHE thickness, respectively, on the predicted enthalpic effectiveness and on the of frost formation. The effectiveness is defined here as

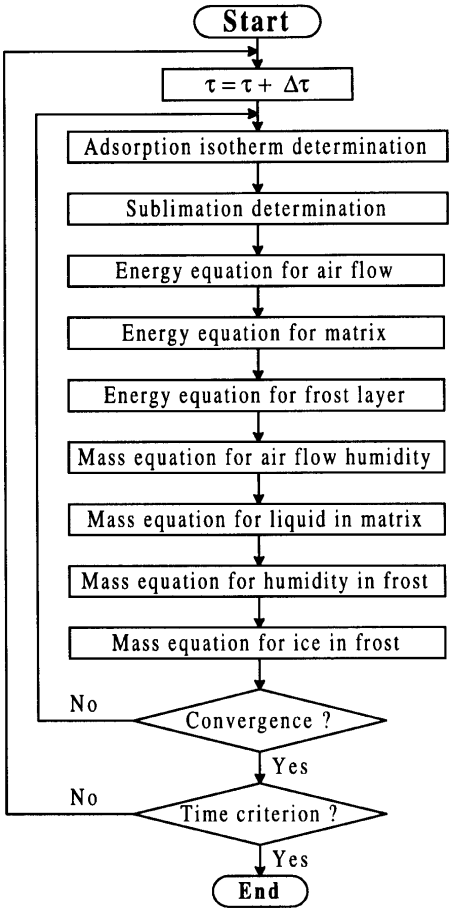

Fig. 6. Numerical algorithm.

$$\varepsilon = \frac{\dot{m}_{cs}(H_{WS} - H_{CS})}{\dot{m}_{min}(H_{WE} - H_{CS})} = \frac{\dot{m}_{we}(H_{WE} - H_{CE})}{\dot{m}_{min}(H_{WE} - H_{CS})} \quad (20)$$

while the frost mass fraction is the ratio of the volume occupied by the frost layer to that of the control volume. Each dot on these figures is the result of a full simulation of the thermal behavior of the RHE. Under normal operating conditions, that is without frosting, increasing the mass flow rate results in an increase of the thermal effectiveness. However, as depicted in Fig. 8a, when frosting occurs, increasing the mass flow rate promotes frost formation, reduces gradually the flow passages and, as a result, the enthalpic effectiveness declines. On the other hand, Fig. 8b shows that increasing the thickness of the wheel reduces frost formation and increases enthalpic effectiveness. Indeed, for a thicker wheel, the heat transfer surface is increased, the temperature gradients are decreased and mass transfer is augmented.

Figure 9 illustrates typical axial temperature profiles for air and for the matrix both in the adsorption and in the regeneration zones ($T_{cs} = -25°C$, $RH_{CS} = 50\%$, $T_{WE} = 22°C$, and $RH_{WE} = 40\%$). It is seen, in the unfrosted portion of the wheel, that the temperature profile is quasi linear. Holmberg [7] suggests that the temperature profile may be approximated by a linear relation over the entire wheel using the inlet conditions. The present results show that this assumption is relevant in the unfrosted region of the wheel but may be inaccurate in the frosted region. Moreover, the bending of the temperature profiles is accentuated as frost builds up.

This figure also reveals that the frosting zone covers about one half of the width of the wheel. This zone is limited by an isotherm corresponding to a matrix temperature of 0°C (freezing set point). Figure 10 shows the isothermal threshold line. It is seen that this line is not horizontal. The coldest point is located at the interface between the regeneration and the adsorption zone (180°) and the hottest spot is situated at 0° (360°). Moreover, the temperature gradients at 0° and 180° are of opposite signs causing uniform thermal expansion of the matrix.

Figure 11 exemplifies the variation of the humidity ratio and of the frost mass fraction (FMF) across the width of the wheel in both the adsorption and the regeneration zones. This figure also illustrates (solid line) the interfacial humidity ratio between the airflow and the cold surface. The behavior of these properties resembles that of the corresponding temperature profiles exhibited in Fig. 9. The profiles are linear in the unfrosted zone and bend slightly in the frosted zone.

The numerical simulations performed also indicate that as the relative humidity of the warm exhaust (WE) increases the matrix temperature in the cold supply (CS) region may augment up to 3°C in the range of the inlet conditions studied (−30–25°C). The sorption phenomenon increases the enthalpic effectiveness and, at the same time, reduces frost formation.

As expected, frosting is strongly dependent on the exhaust air relative humidity RH_{WE} and on the cold supply temperature T_{cs}. The frost mass fraction is elucidated in terms of both these parameters in Fig. 12a. The black region represents the operating conditions without frost formation. The boundary of this region may be seen as the frosting limit. As an example, for $T_{CS} = -20°C$ and $RH_{WE} = 15\%$, frosting will not occur, while for $T_{CS} = -15°C$ and $RH_{WE} = 30\%$, it will.

From a design and operating point of view, it is of the utmost importance to control frost formation in the RHE. Its overall performance is also influenced by the time duration between two consecutive defrosting cycles. Frequent defrostings means that the thermal wheel is unoperative and, on the other hand, insufficient defrosting deteriorates its thermal performance and may, in the long run, damage it. It is therefore necessary to estimate the amount of frost formed under various harsh conditions and also the time required before a defrosting action must be taken.

Figure 12b illustrates the effect of time on the frosting

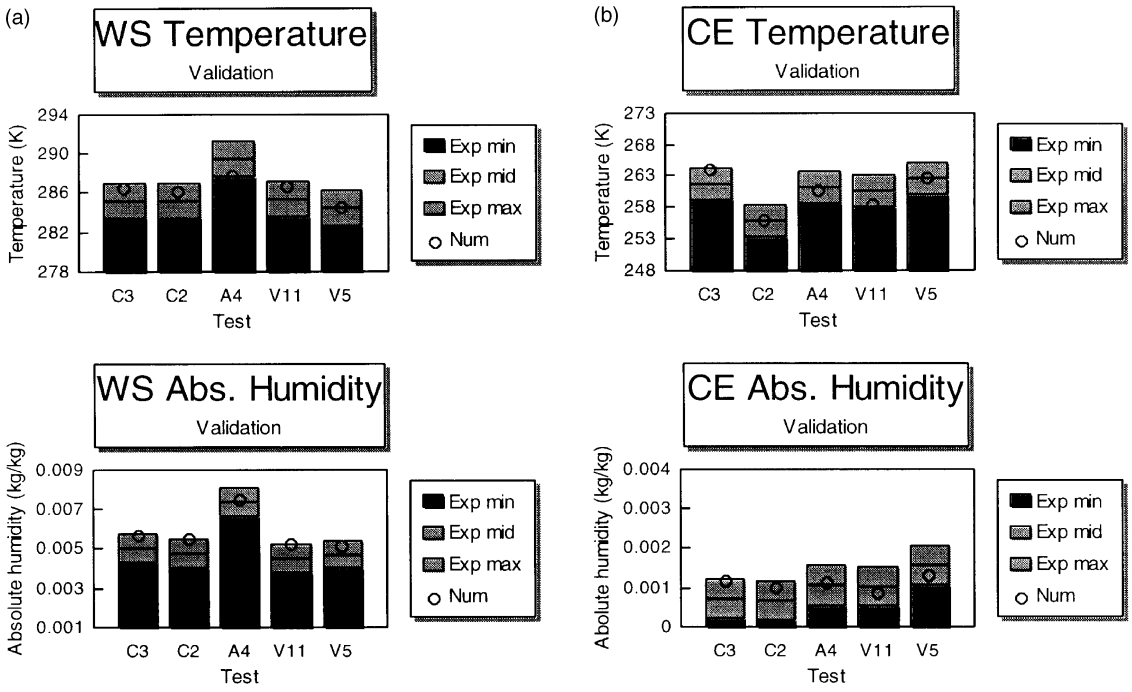

Fig. 7. (a) Validation of the model: temperature data. (b) Validation of the model: humidity data.

Table 4
Experiments for the validation of the model

Test ID	T_{CS} [K]	W_{WE} [kg_v/kg_a]	T_{WS} [K]	W_{WS} [kg_v/kg_a]	T_{CE} [K]	W_{CE} [kg_v/kg_a]
PERC4	258.1	0.0092	285.8	0.0068	263.3	0.00109
PERC3	257.7	0.0079	285.2	0.0050	261.7	0.00097
PERC2	251.2	0.0072	285.1	0.0048	255.9	0.00070
PERA4	249.2	0.0094	289.5	0.0074	261.2	0.00110
VEN11	248.2	0.0065	285.2	0.0045	260.7	0.00100
VEN05	248.2	0.0065	284.4	0.0047	262.5	0.00160
PERE2N	265.0	0.0070	285.4	0.0048	267.1	0.00110
PERE4N	265.9	0.0076	286.8	0.0050	269.3	0.00100

For these experiments T_{WE} was maintained at 295.2 K (with an experimental uncertainty of ± 0.3 K) and W_{CS} was fixed at 0.00023 kg vapor/kg air (with an experimental uncertainty of ± 0.0005 kg vapor/kg air).

limit. Examination of this figure reveals that after 30 min of operation frosting may occur only under severe conditions (for T_{CS} under $-20°C$ or RH_{WE} over 40%). As time passes however, the likelihood of frosting augments and stabilizes and an operating period of about 2 h may be seen as the upper limit. This chart may prove very useful to establish control strategies for defrosting RHE. For instance, if $T_{CS} = -15°C$ and $RH_{WE} = 40\%$, one may envisage to preheat the cold supply air every 30 min to prevent frosting. On the other hand, if $T_{CS} = -20°C$ and $RH_{WE} = 25\%$, cyclic preheating would be necessary only every 2 h.

The effect of the exhaust air relative humidity on the period of time needed for complete frosting is depicted in Fig. 13. As expected, this time decreases as the cold supply temperature decreases and as the relative humidity augments. The relative humidity is, however, the dominant parameter. Also, this figure illustrates the fact that rotary heat and mass exchangers often present very slow frost formation on their surface. This figure reveals that

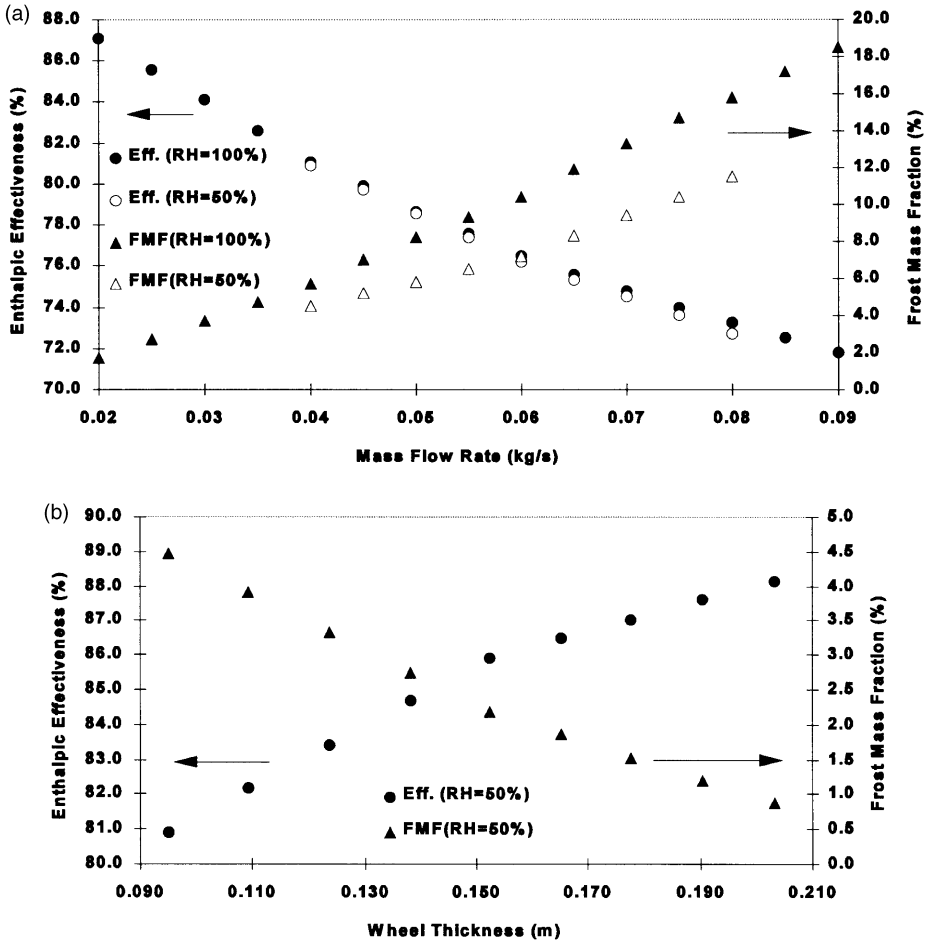

Fig. 8. (a) Effect of the mass flowrate on the enthalpic effectiveness (Eff.) and on the frost mass fraction (FMF). (b) Effect of wheel thickness on the enthalpic effectiveness (Eff.) and on the frost mass fraction (FMF).

it will take more than 26 days of constant operation to reach complete frosting at T_{CS} over $-15°C$ with W_{WE} under 0.004 kg_v/kg_a (corresponding to interior conditions of 22°C and RH_{WE} of 25%). These are typical winter conditions in northern climates and the figure of 22°C confirms the high level of tolerance of the RHE toward frosting. But this figure also reveals, that in extreme conditions, say $-25°C$ and lower with more than 0.005 kg_v/kg_a, frosting may build up very quickly. In less than 2 days, the RHE may not be operational in these conditions.

Clearly, the frosting limit is influenced by the geometry of the RHE and is linked to the efficiency of the heat and mass exchanger. The results emphasize the importance of the operating conditions and of the thermodynamic properties of the humid air. An important issue, for the design of HRV or RHE, is to obtain a less restrictive frosting limit. This parametric study has shown that optimization of the RHE is not only possible, but is also required in order to ensure that proper control strategies are implemented for operation in cold climates.

5. Conclusion

Frost formation in rotary heat and mass exchangers was investigated both experimentally and numerically. Experiments conducted with a refrigerated flat plate have revealed that glazed frost, whose density and thermal conductivity are higher than that of rough frost, prevails in rotary exchangers operating in cold climates. A mathematical model was next developed to predict the thermal behavior of the rotary exchanger. The transient three-dimensional model was validated with experimental data for the cold exhaust temperature and humidity and the warm supply temperature and humidity.

Results indicate that the absolute humidity is the prevailing parameter for characterizing the frosting phenom-

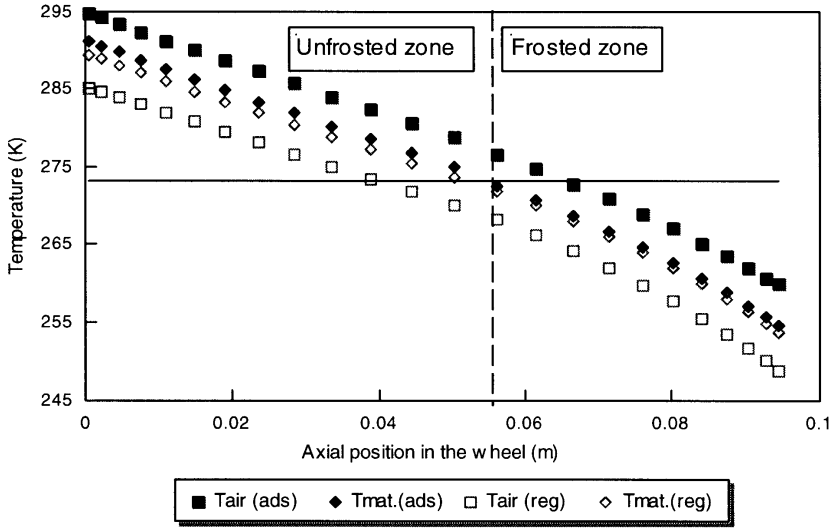

Fig. 9. Axial air and matrix temperature profiles in the wheel.

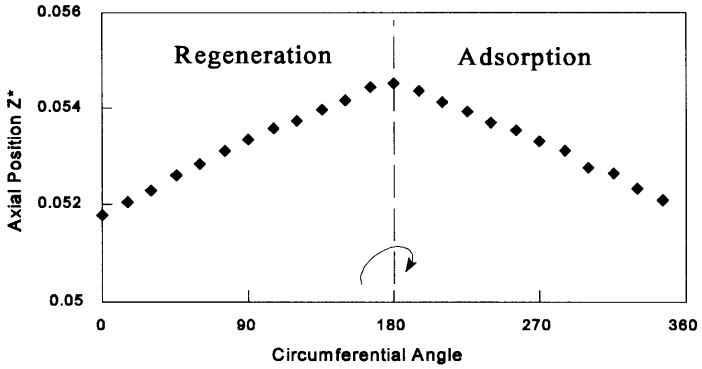

Fig. 10. Frosting zone limit (freezing set point isotherm: 0°C).

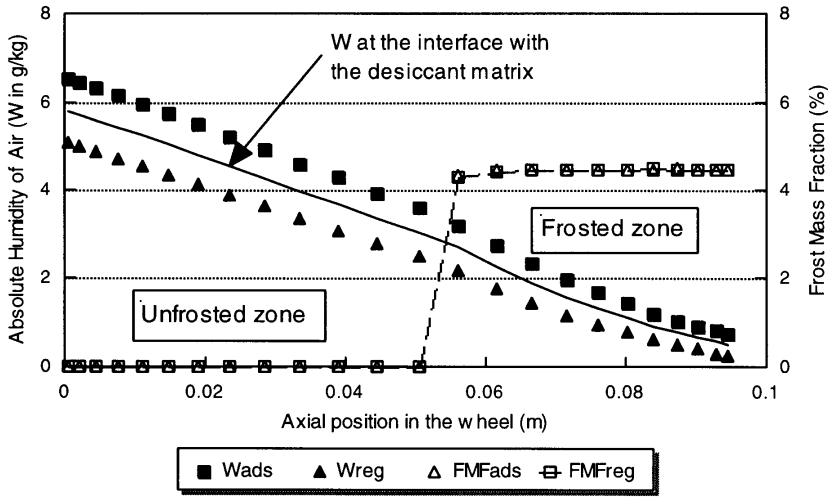

Fig. 11. Absolute humidity and frost mass fraction vs axial position.

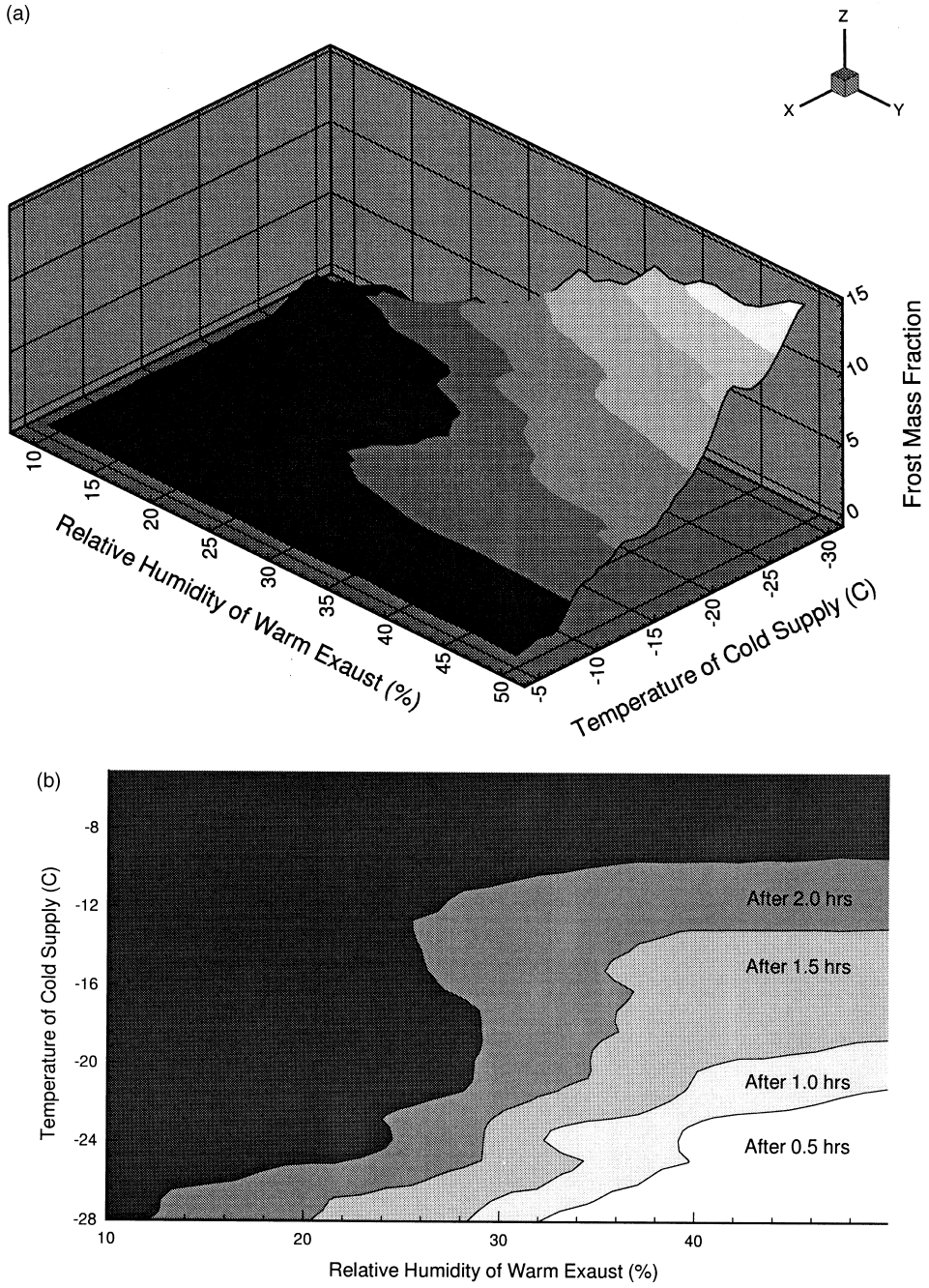

Fig. 12. (a) Frost mass fraction vs relative humidity and cold supply temperature. (b) Effect of time on the frosting limit.

enon. A frost mass fraction chart was established in terms of the relative humidity of the warm exhaust stream and of the temperature of the cold supply stream. Unlike the widely retained assumption, it was shown that the absolute humidity and the temperature of both air flows vary nonlinearly in the frosted zone.

This study has also shown the link between frosting conditions and effectiveness. using RHE for ventilation energy recovery, it is possible to maintain higher efficiency and lower frosting limits. It is clear that traditional control strategies for operating RHE in cold climates (fixed control based on the freezing point or on fixed time period) are inadequate and may even be damaging to the desiccant materials. proper adaptive

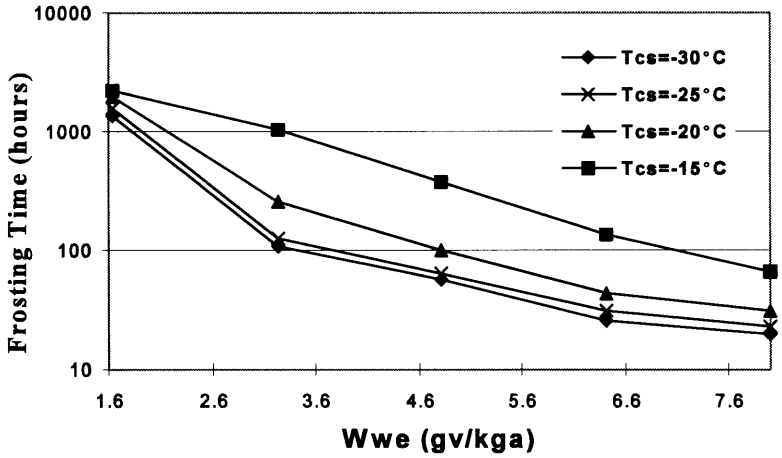

Fig. 13. Frosting time vs warm exhaust relative humidity and cold supply temperature.

frost control strategies resting on the present study will have to be developed and implemented for the successful use of the RHE in cold climates.

Acknowledgements

The authors would like to thank the Natural Sciences and Engineering Research Council of Canada and the Fonds pour la Formation de Chercheurs et l'Aide à la Recherche du Québec (FCAR) for their financial support. They also acknowledge the technical support from the Energy Diversification Research Laboratory of Natural Resources Canada.

Appendix

Expressions for the coefficients a and b in equation (19)

$$a_N = D_n A(|P_n|) + \|-F_n, 0\|$$
$$a_S = D_s A(|P_s|) + \|F_s, 0\|$$
$$a_E = D_e A(|P_e|) + \|-F_e, 0\|$$
$$a_W = D_w A(|P_w|) + \|F_w, 0\|$$
$$a_T = D_t A(|P_t|) + \|-F_t, 0\|$$
$$a_B = D_b A(|P_b|) + \|F_b, 0\|$$
$$a_P^0 = \rho_P^0 \frac{\Delta x \Delta y \Delta z}{\Delta t}$$
$$b = S_c \Delta x \Delta y \Delta z + a_P^0 \phi_P^0$$
$$a_P = a_N + a_S + a_E + a_W + a_T + a_B + a_P^0 - S_P \Delta x \Delta y \Delta z.$$

D is the diffusion conductance ($\Gamma/\partial x$), F is the mass flux (ρv) and P is the Peclet number, i.e. $P = F/D$. The function $\|x, y\|$ gives the maximum value between x and y and the function $A(|P|)$ is given by

$$A(|P|) = \|0, (1 - 0.1|P|)^5\|.$$

References

[1] E. Phillips et al., Comparison of freezing control strategies for residential air-to-air heat recovery ventilators, ASHRAE Transactions 95 (2) (1989) 484–490.
[2] Y. Mercadier, T. Duong, F., Lagacé, Dynamic performance of a cross flow heat recovery ventilator operating under frost conditions, Proceedings of the Fourth International Symposium on Thermal Engineering and Science for Cold Regions, Hanover, NH, 1993, pp. 113–121.
[3] R.B. Holmberg, Prediction of condensation and frosting limits in rotary wheels for heat recovery in buildings, ASHRAE Transactions 99 (1) (1993) 64–69.
[4] S. Pfeiffer, H. Hübner, Untersuchungen zum Einfrieren von Regenerativ-Wärmeübertragern, Ki Klima-Kälte-Heizung, October 1987, pp. 449–452.
[5] D.W. Ruth, D.R. Fisher, H.N. Gawley, Investigation of frosting in rotary air-to-air heat exchangers, ASHRAE Transactions 81 (2) (1975) 410–417.
[6] M.H. Attia, N.S. D'Silva, On the thermal characteristics and response behavior of residential rotary regenerative heat exchangers, Proceedings of the 14th Sem. International Cent. Heat and Mass Transfer, Hemisphere Publishing Corp., 1983, pp. 599–611.
[7] G. Stiesh, S.A. Klein, J.W. Mitchell, Performance of rotary heat and mass exchangers, HVAC & R Research, ASHRAE 1 (4) (1995) 308–324.
[8] Y. Hayashi, et al., Study of frost properties correlating with frost formation types, Journal of Heat Transfer, Transactions of the ASME 99 (1977) 239–245.
[9] Y.X. Tao, R.W. Besant, Y. Mao, Characteristics of frost growth on a flat plate during the early growth period,

Proceedings of ASHRAE Transactions Symposia, Atlanta, 1993, CH-93-2-2, pp. 746–753.

[10] I. Tokura et al., Study on properties and growth rate of frost layers on cold surfaces, Journal of Heat Transfer, Transactions of the ASME 105 (1983) 895–901.

[11] R. Östin, S. Andersson, Frost growth parameters in a forced air stream, International Journal of Heat and Mass Transfer 34 (4) (1991) 1009–1017.

[12] S. Bilodeau, Modélisation expérimentale et numérique de la formation du givre dans le roues enthalpiques, Ph.D. thesis, Université de Sherbrooke, Québec, Canada, 1998.

[13] J.M. Delhaie, Basic equations for two-phase flow modeling, in: A.E. Bergles et al. (Eds.), Two-Phase Flow and Heat Transfer in the Process Industries. Hemisphere Publishing Corp., Washington, DC, 1981, pp. 41–97.

[14] S.V. Pantakar, Numerical Heat Transfer and Fluid Flow, McGraw-Hill Book Co., New York, 1980, p. 197.

[15] S. Bilodeau, P. Brousseau, M. Lacroix, Y. Mercadier, Modelling of a frost formation in rotary heat regenerator, Proceedings of the Fifth International Symposium on Thermal Engineering in Cold Regions, Ottawa, May 1996, pp. 373–378.